Materials Characterization Volume 150, April 2019, Pages 174-183

Microstructure, dynamic restoration and recrystallization texture of Sn-Cu after rolling at room temperature

Guangyu Liu, Shouxun Ji*
Brunel Centre for Advanced Solidification Technology (BCAST), Brunel University London, Uxbridge, Middlesex UB8 3PH, United Kingdom

ABSTRACT
A hypoeutectic Sn-0.5wt%Cu alloy was prepared by casting and subsequent rolling under a moderate strain rate (3.5×10^{-2} s $^{-1}$) at room temperature. The microstructural evolution including boundary formation, dynamic restoration, twinning, and recrystallization texture was examined using the electron back-scattered diffraction (EBSD) technique, aiming to understand the deformation mechanisms of the Sn-Cu system serving under external stress. The results confirmed that a bimodal grain structure was well established, which could be ascribed to the dislocation activities and dynamic restorations including dynamic recovery (DRV) and dynamic recrystallization (DRX). The Cu_6Sn_5 particle-stimulated nucleation (PSN) was found as the major mechanism of DRX, which was also the dominant factor leading to the formation of ⟨001⟩//RD oriented nuclei. Moreover, DRX nuclei formed along the existing boundaries, resulting in the formation of necklace structure via continuous dynamic recrystallization (CDRX). Twinning involving {301} and {101} twin configurations was identified as the additional mechanism of effective deformation.

1. Introduction

For years, due to the environmental and human health concerns over the toxicity of lead (Pb) [1], lead-free tin (Sn)-based alloys have been extensively used as the substitutes of Pb-based alloys in the application of conventional soldering technology [2] and linear explosive products [3]. Among them, Sn-Cu alloys are particularly noticeable for packaging, solder joints, and electronic assembles due to the low cost and decent comprehensive properties [4]. Moreover, Sn-Cu systems have also been considered as cladding materials for linear explosive devices due to the good workability, relatively high density, and small thermal neutrons absorption in high radiation environments [5]. For example, Rodney et al. [6] have reported that Sn-Cu-Sb and Sn-Cu-Bi can be used as the outer sheathing materials in ignition cords, mild detonating cords, and linear shaped charges. Huang et al. [7] have claimed the use of Sn-(0–20) wt% Cu as linear initiating explosive devices. Recently, Sn-(0.3–1.0) wt%Cu alloys after processing at ambient temperature have been studied and proposed as the cladding materials in the detonating and explosive cords used for the clearance of aircraft canopies, due to nonwork-hardening and easy-manufacturing through rolling, extrusion, and drawing [8].

The feasibility and reliability of the Sn-Cu alloys for the application as the sheathing of linear explosive device are highly dependent on the mechanical behaviour and microstructural evolution that occur interactively during the manufacturing process and its service lifetime [8]. Assessment of the mechanical properties of Sn-Cu alloys has been widely performed and previous researches have confirmed a combination of good tensile strength and ductility of the Sn-0.7wt%Cu alloy [9,10]. Pang et al. [11] investigated the low cycle fatigue performance of Sn-0.7wt%Cu and confirmed their superior fatigue performance compared to Sn-37wt%Pb alloy. Also, Wu et al. [12] studied the creep behaviour of Sn-0.7wt%Cu alloy at different temperatures ranging from 303 to 393 K, suggesting that the creep rates were controlled by the dislocation-pipe diffusion in the Sn matrix.

Despite of the mentioned studies on the mechanical performances of Sn-Cu alloys, limited work has been done for the exploration of detailed deformation mechanisms during processing, which is particularly important in the manufacturing of the linear explosive device when the Sn-Cu sheathing is simultaneously drawn with an explosive core in the strict conditions for aerospace applications. The explosive core is generally made of pentaerythritol tetranitrate (PETN), cyclotrimethylenetrinitramine (RDX), cyclotetramethylenetetranitramine (HMX), or hexanitrostilbene (HNS) [13]. Additionally, the interaction between the explosive core and the metal sheathing matters as well in the manufacturing

process, especially under the condition that intense deformation heat may be generated. These are closely associated with the deformation mechanisms of the sheath material.

Although the macrostructure variation of Sn-Cu alloys involving the Cu6Sn5 intermetallic phase and grain refinements were investigated in our previous work [8], a comprehensive examination of micro-scaled microstructure features involving the evolutionary process of the dislocations and grain boundaries, or with respect to the microstructural homogeneity/inhomogeneity, is still highly desirable. Because when it comes to practical performance of the linear explosive devices, the homogenous structure introduces smoother jet particles during jetting process of the sheath, benefiting the penetration performance, while the inhomogeneity in structure gives rise to unsmoothed jetting particles which are detrimental to cutting efficiency.

Therefore, the present work aims to explore the microstructural features and thorough deformation mechanisms of the Sn-0.5wt%Cu alloy after rolling at room temperature. The microstructure, grain boundaries, dynamic restorations, twining, and recrystallization texture has been characterized through the electron backscattered diffraction (EBSD) technique. The emphasis has been focused on the dynamic recrystallization (DRX) phenomenon and the effect of Cu6Sn5 particles on the microstructure. The results have provided the deformation database as the reference for the Sn-based alloys, especially for those comprising the Sn matrix and the second-phase particles such as Sn-Ag systems in the similar applications.

2. Experimental

Sn and Cu ingots with commercial purity (99.9%) were used as the raw materials. Prior to melting, each element was weighed to a specified ratio with specified burning loss compensation. A certain mass of melt was prepared in a stainless-steel crucible coated with Al2O3 coatings and the melting was conducted in an electric resistance furnace. After melting, the melt at 360 °C was manually poured into a tool steel mold (preheated at 200 °C) to form the casting bar which was approximately 300 mm long and had a trapezoid-shaped cross-section of 20 × 16 × 16 mm. The chemical composition of the experimental Sn-0.5wt%Cu alloy was analyzed by the inductively coupled plasma atomic emission spectroscopy (ICP-AES, ARCOS, Simultaneous ICP Spectrometer, SPECTRO Analytical Instruments GmbH, Germany), as shown in Table 1.

The Sn-0.5wt%Cu casting bars were then homogenized at room temperature for two weeks. Afterwards, Sn-0.5wt.%Cu bars were rolled at room temperature using a rolling machine (Durston FSM200 Rolling Mill, UK). The nominal diameter of roller is 110 mm. There are 24 square grooves on the roller surface to form square rolled bars. The casting bar was rolled continually, to a cross-section area ratio of the rolled product to the casting product of 0.13. The machine was operated at a rolling speed of 5 rev min−1, corresponding to the rolling velocity of 3.1 × 10−2 m/s. The rolled bar was defined as rolling direction (RD), transverse direction (TD), and normal direction (ND), respectively. More details on the rolling procedure can be referred to our previous work [8]. Microstructural characterizations on both transverse cross-section and longitudinal cross-section were conducted for the as-rolled samples using backscatter electrons (BSE) observation and electron backscattered diffraction (EBSD) technique in a Zeiss Supra 35VP field emission scanning electron microscopy (SEM) equipped with Energydispersive X-ray spectroscopy (EDX) working at 20KV. The surface preparation for EBSD was conducted by SiC paper grinding and mechanical polishing by 0.05 μm colloidal silica suspension. The EBSD scanning step sizes were in the range from 1.0 to 2.0 μm under different magnifications. The microstructure data were analyzed using TSL OIM 7.3 software to acquire detailed information on the grain orientation and boundary characteristics, and to identify grains with internal misorientations smaller than 2°. The clean-up method to orientation maps was performed using Grain CI Standardization (Grain Tolerance Angle: 3, and Minimum Grain Size: 2), exerting very limited modification on original/actual results.

3. Result and discussion

3.1. Solidification microstructure of the Sn-0.5wt.%Cu alloy

Fig. 1 (Fig. 1a and b is optical micrographs; Fig. 1c, d, and e is backscattered SEM images) shows the morphology, size and distribution of the primary β-Sn phase and the intermetallic phase in the as-cast microstructure of the Sn-0.5wt.%Cu alloy. The microstructure comprised the primary β-Sn phase with dendritic morphology and eutectic (Fig. 1a, b and c). The grain size of the β-Sn phase was measured in the range of 100–300 μm. It was observed from Fig. 1d and e that the intermetallic phase was characterized as Cu6Sn5, showing a needle-like morphology with the diameter of 1–3 μm and the length of 10–20 μm [8]. Note that the distinct morphology of Cu6Sn5 phase shown in Fig. 1d and e was because the axes of individual Cu6Sn5 intermetallic phase were differently oriented in the β-Sn matrix. The area fraction of SnCu6Sn5 eutectic was proximately 33%. Note that no other intermetallic phases such as Cu3Sn were observed in the structure. The solidification path and microstructural evolution can be understood through the equilibrium phase diagram of Sn-Cu system [14]. When the Cu content is 0.5 wt%, the Sn-Cu alloy is solidified as a hypoeutectic alloy, following the phase transformation: L → L + primary β-Sn → primary βSn + eutectic (Sn + Cu6Sn5).

Fig. 2 shows the EBSD map and the corresponding grain boundary misorientations distribution of the as-cast Sn-0.5wt.%Cu alloy with the RD along the axis of casting bar. Clearly, a trace of high-angle grain boundary (HAGB), marked by the yellow-colour arrow, with a great length was extended from the top right corner to the bottom left corner of the map, separating the two neighbouring β-Sn grains (Fig. 2a). Numerous low-angle grain boundaries (LAGBs) or sub-grain boundaries were observed interior the β-Sn grains, such as those highlighted by the white-colour arrows in Fig. 2a. Majority of the boundaries were identified as LAGBs, as shown in Fig. 2e, indicating the existence of slight lattice distortion in the as-cast microstructure. Numerous coarse intermetallic particles of Cu6Sn5 were embedded into the individual β-Sn grain, as indicated by image quality map (Fig. 2b) and the phase map (Fig. 2c). These embedded Cu6Sn5 particles were deemed to cause lattice distortions of the β-Sn matrix surrounding them. The lattice distortion in the Sn matrix at the vicinity of the Cu6Sn5 particles is very likely in association with the difference in coefficient of thermal expansion of the two phases (Cu6Sn5 and surrounding Sn phases). After the two individual phases solidified, they continued to cool down to the room temperature. In this process, the slight volume variation of the two phases occurred in a difference pace, which might cause the formation of mismatch or defects such as voids and dislocations in the interface between Cu6Sn5 and surrounding Sn matrix. In this way, the micro-strain energy resulted from the different extent of bulk volume variation can be relieved. In those areas near large-sized Cu6Sn5 particles or near Cu6Sn5 clusters, the defects in the interface might not sufficiently high in energy to release the distortion energy, consequently, severer lattice distortions in the Sn matrix further away from the Cu6Sn5 particles were likely formed to compromise the increased distortion energy.

Table 1 Chemical composition of the experimental Sn-0.5wt%Cu alloy analyzed by inductively coupled plasma atomic emission spectroscopy (ICP-AES).

Alloys	Sn (wt.%)	Cu (wt.%)	Zn (wt.%)	Ni (wt.%)	Bi (wt.%)	Fe (wt.%)	Sb (wt.%)	As (wt.%)	Cd (wt.%)
Sn-0.5Cu	Rem	0.49	0.03	0.01	0.015	0.01	0.02	0.014	0.006

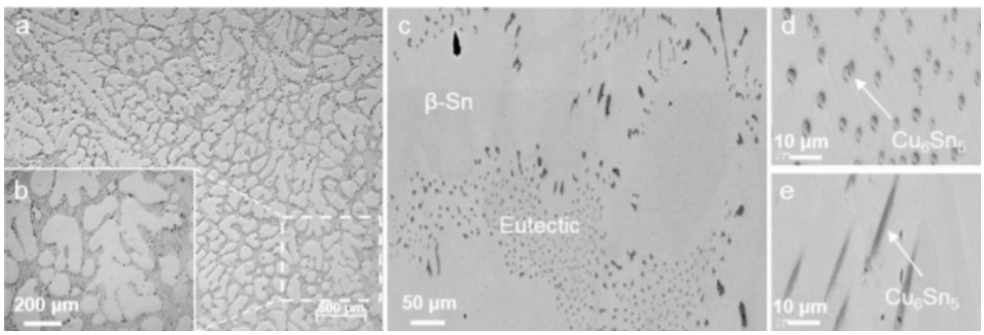

Fig. 1. (a, b) Optical micrographs and (c, d, e) backscattered SEM micrographs showing the morphology and size of the primary β-Sn dendrites, eutectic, and intermetallic phase in the as-cast Sn-0.5wt.%Cu alloy.

3.2. Microstructure of the Sn-0.5wt.%Cu alloy after rolling

Fig. 3 presents the microstructure on the transverse and longitudinal cross-sections of the Sn-0.5wt.%Cu alloy after rolling. The size of primary β-Sn dendrites was dramatically decreased and the microstructure became much finer (Fig. 3a). The primary β-Sn phase and the SnCu6Sn5 eutectic region were severely deformed along the rolling direction, resulting in the formation of elongated β-Sn phase and eutectic regions (Fig. 3b). Inset in Fig. 3 shows the size and morphology of Cu6Sn5 intermetallic phase after rolling. The original Cu6Sn5 intermetallic rods were broken into smaller segments and separated each other in the β-Sn matrix. The size of Cu6Sn5 intermetallic phase was ranged from 1 to 6 μm with an average of 3 μm. More details of the structural evolution of the Cu6Sn5 intermetallic phase can be referred to our previous work [8].

3.2.1. Bimodal grain structure

Fig. 4 shows the IPF map, grain size distribution, and grain boundary misorientations distribution on the ND + TD plane of the Sn0.5wt.%Cu alloy after rolling. A considerable change in the microstructure was observed in comparison with the as-cast structure. It was clearly seen from Fig. 4a that a predominant bimodal grain structure was well established, with an alternatively distributed fine grains and coarse grains. The fine grains were < 30 μm with near-equiaxed grain structures, while the coarse ones were in the range of 50–150 μm and displayed irregular-shaped grain structures instead.

According to the statistical measurements, the fine grains accounted for > 97% of total number of grains (Fig. 4b) and the coarse grains represented extremely limited numbers (< 3%). It was seen from Fig. 4c that the high-angle grain boundaries (HAGBs) with misorientations higher than 15° were evenly distributed in the whole misorientations range except the fact that a group of near-60° misorientation angles constituted an exceptional increased fraction. The HAGBs took up > 78% of total grain boundaries. The near-60° misorientation angles were associated with the twinning configurations in the β-Sn structure, {301} and {101} type twins, rotation about a common ⟨100] axis [15]. The {301} twining system has been usually observed in the {301} twin plane with 103 twinning shear direction

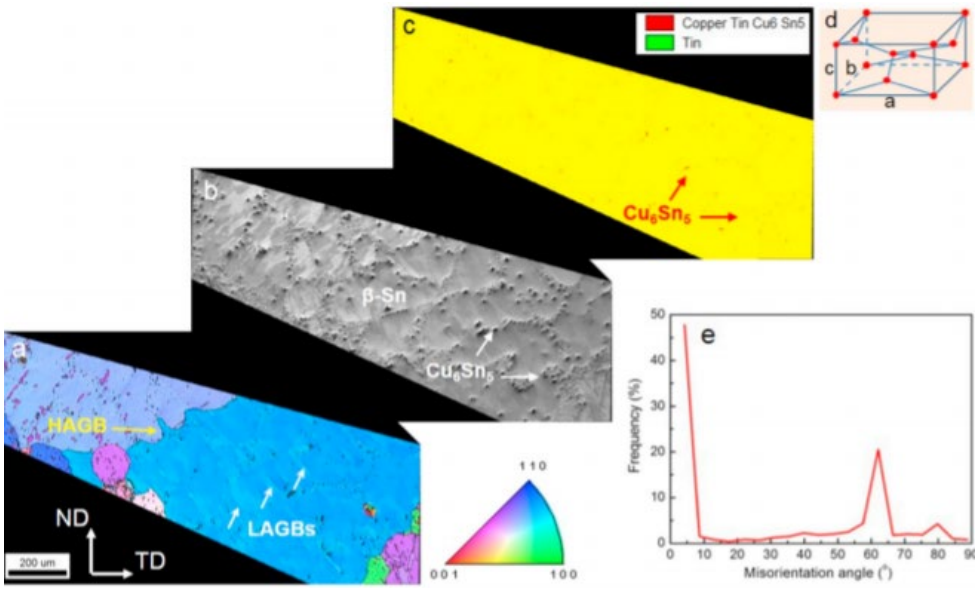

Fig. 2. EBSD maps and grain boundary misorientations distribution of the as-cast Sn-0.5wt.%Cu alloy with the RD parallel to the axis of the casting bar. (a) Inverse pole figure (IPF) map, (b) image quality (IQ) map, (c) phase map, (d) the crystal cell of β-Sn with body centred tetragonal (BCT) structure, and (e) the grain boundary misorientations distribution extracted from (a). The high-angle grain boundaries (HAGBs, > 15°) signified by thick black lines, and the light white lines presenting the low-angle grain boundaries (LAGBs, 2–15°). but the {101} twinning system was rarely seen in the {101} twin plane with 101 twinning shear direction [16].

Based on the perceived characteristics of the structure in the asrolled Sn-0.5wt.%Cu alloy including the bimodal grain structure, highfractioned HAGBs and the equiaxed-shape grains, it was suggested that the microstructure after rolling exhibited a typical hot-processing structure with the grains being partially or fully recrystallized. It has been well documented that conventional dynamic recrystallization (often referred as discontinuous dynamic recrystallization, DDRX) takes place during straining as long as the working temperature is above 0.5Tm [17–19]. In the Sn-0.5wt.%Cu alloy, the rolling at ambient temperature was considered as hot working because the processing temperature at 293 K was higher than 0.5Tm [8]. Dynamic recrystallization was thus one of the dominant features during deformation and could play an essential role in final microstructure establishment.

3.2.2. Dynamic restoration

Fig. 5 shows the image quality (IQ) combined with the grain orientation spread (GOS) map of an enlargement of the highlighted region in Fig. 4a. GOS map is deemed a useful tool to evaluate the in-grain misorientation. The GOS value is the average deviation between the orientation of each individual measuring point within a grain and the average grain orientation calculated for the specific grain [20]. It provides a quantitative description of the crystallographic orientation gradients in individual grains. As deformed grains possess internal orientation gradients, they give rise to relatively high GOS values. However, the recrystallized grains possess no or very limited in-grain orientation gradients, and thus produce low GOS values. Here the grains with GOS values smaller than 1.5° (colour scaled in Fig. 5) can be reasonably considered as the recrystallized grains, and those with no colour scale represent the GOS values larger than 1.5°, which can be treated as non-recrystallized grains.

3.2.2.1. Dynamic recovery (DRV). The LAGBs at 2–15° and the formation of sub-grains were seen interior the non-recrystallized grains, as represented by the black arrows in Fig. 5. This indicates that the dynamic recovery (DRV) has occurred under rolling. The basic mechanisms of DRV involve dislocation climbing and gliding, which result in the formation of LAGBs [21]. DRV is greatly dependent on the deformation conditions, such as strain rate and temperature. At high temperature, dislocation climbing and cross-slip can occur readily, DRV is thus rapid and extensive. In the present study, β-Sn processes multiple preferred slip systems at room temperature, which has been identified as {100) ⟨001], {110) ⟨001], and {100) ⟨010] [22,23]. On top of the preferred slip systems, depending on the crystal orientation, Sn can access up to 10 different slip systems [24]. Therefore, multiple slip systems can offer great potential for dislocation generation under strain. During the initial stage of rolling, an increase in the flow stress results from the dislocations interaction and multiplication. The dislocation density and the stored energy increase with further straining, leading to the increase of the driving force for the recovery. Consequently, the microstructure of low-angle grain boundaries or subgrains develops. On the other hand, the hot deformation and the relatively low strain rates facilitate DRV. At high temperatures, slip systems which are not activated at low temperatures may become active and cause the increase in the number of operating slip system and the deformation therefore becomes homogeneous. In this case, DRV occurs more easily than DRX does. The relatively low strain rates further increase the time for dislocations motion, interaction and annihilation, which can benefit the formation of DRV as well.

Given that the DRV was largely observed, DRX was still the noticeable restoration phenomenon since the large regions of inhomogeneity from Cu_6Sn_5 particles and original grain boundaries in association with the severely strain-accumulated areas could be the sites for initiating the DRX. Moreover, from Fig. 5, it is worthy pointing out that the recrystallized fine grains can be generally classified into three categories: (1) those with aggregated distribution highlighted by white-colour ellipse, (2) those sparsely distributed in the grain interior, as marked by yellow-colour ellipse, and (3) those formed at the vicinities of the grain boundaries (marked by black-colour ellipse). This is ascribed to the different recrystallization mechanisms mainly involving the particle-stimulated nucleation (PSN) and the boundary associated nucleation, which will be interpreted individually in the following sections.

3.2.2.2. Particle-stimulated nucleation (PSN). Fig. 6 shows the image quality (IQ) map and the phase map of a region extracted from Fig. 5. Clearly, the fine grains tended to form in the regions where Cu6Sn5 intermetallic particles were densely spaced, as highlighted by the ellipses in Fig. 6. However, particles were scarcely observed in the interior of coarse grains, which could be represented as the particle-free regions. This phenomenon is the clear indication of the particlestimulated nucleation (PSN). It has been well documented that the coarse (> 1 μm) second-phase particles, especially those widely spaced particles, can promote dynamic recrystallization via the mechanism of particle-stimulated nucleation [25–27]. In the present study of Sn0.5wt.%Cu alloy, the Cu6Sn5 particles with the sizes over 1 μm in diameter [8] meet the criteria of nucleation initiation in terms of the particle dimensions. Moreover, PSN has been proposed on the basis of that the enforced strain gradient at the vicinity of a less- or nondeformable particle can create a region of high-density dislocations and large orientation gradients, namely particle deformation zone or PDZ.

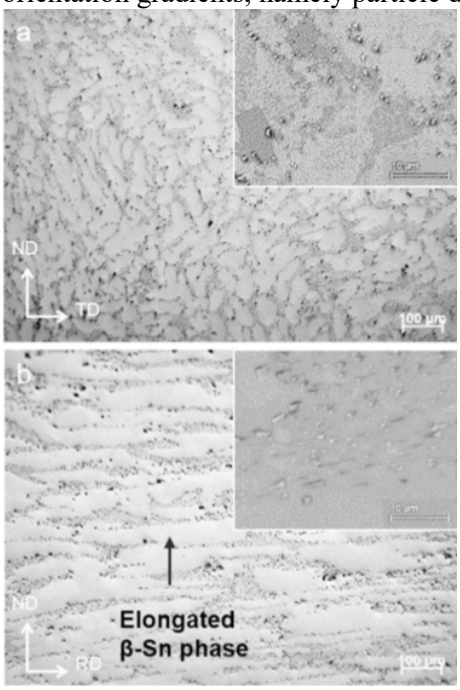

Fig. 3. Optical micrographs showing the microstructure of the rolled Sn-0.5wt %Cu alloy, (a) transverse cross-section, and (b) longitudinal cross-section. Insets are the SEM micrographs showing the corresponding morphology and size of the Cu6Sn5 particles.

The PDZ can be the site for nucleation of recrystallization. Therefore, PSN is generally regarded as an effective approach to accelerate recrystallization and to obtain fine grains in the microstructure. Fig. 7 shows the typical EBSD orientation maps of the Sn-0.5wt.%Cu alloy after rolling, in which Fig. 7a and b presents the IQ + IPF map on the RD + TD plane and the IPF map on the TD + ND plane, respectively. The grain was elongated along the RD, into which numerous sparsely spaced Cu6Sn5 particles were embedded (Fig. 7a). The PSN nuclei/grains were clearly perceived near these Cu6Sn5 particles, as demonstrated by the large lattice orientation differences between the nuclei and the surrounding matrix (highlighted by the red-colour ellipses in both Fig. 7a and b). In brief, the particle-stimulated nucleation could be summarised as the following successive process: first, the dislocation multiplication or accumulation developed near the Cu6Sn5 particles; then, LAGBs or sub-grains formed owing to highly accumulated dislocations; finally, new nuclei with HAGBs were established. Under strain, the hard Cu6Sn5 particles were considered as the deformation heterogeneities which could act as the barriers for the motion of the active dislocations. Therefore, the high density mobile dislocations were pinned and accumulated to enforce the strain gradient. With further progress of straining, the highly accumulated dislocations interact each other through dislocation tangling or rearrangement, leading to the formation of LAGBs or sub-grains. Examples of the resulting LAGBs/sub-grains near the Cu6Sn5 particles can be found on

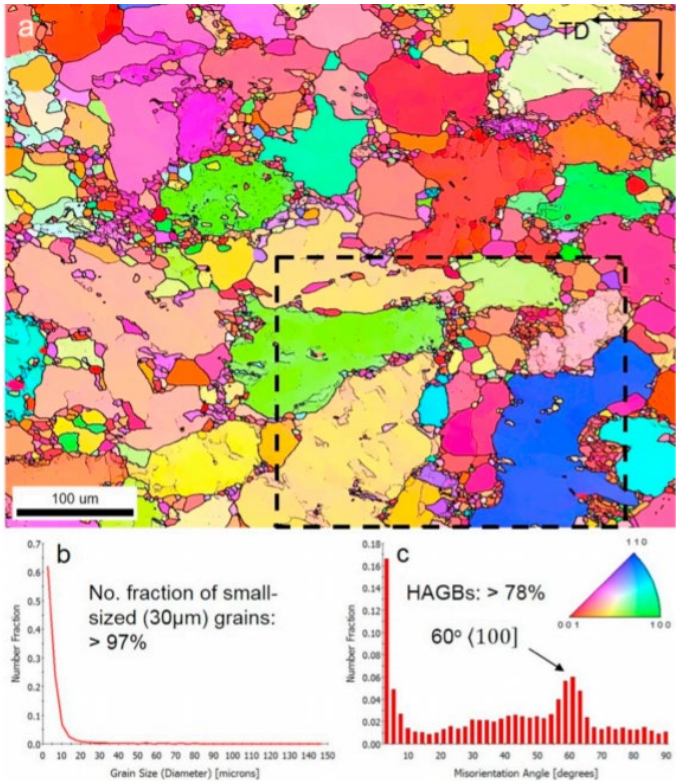

Fig. 4. (a) Inverse pole figure (IPF) map of the rolled Sn-0.5wt%Cu alloy with its corresponding IPF referring to RD direction, (b) corresponding grain size distribution, and (c) grain boundary misorientations distribution. The HAGBs (> 15°) and LAGBs (2–15°) presented by thick and thin black lines, respectively.

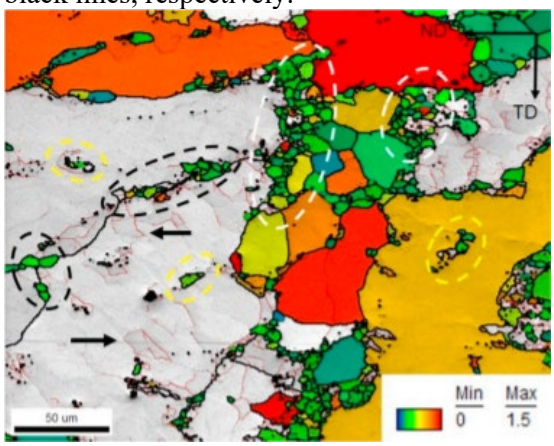

Fig. 5. Superposed image quality (IQ) and grain orientation spread (GOS) maps of the rolled Sn-0.5wt%Cu alloy, showing the recrystallized grains differentiated by selecting GOS values smaller than 1.5°. The HAGBs (> 15°) and LAGBs (2–15°) presented by thick and thin black lines, respectively.

both the longitudinal plane and the transverse plane, as shown by the dotted black arrows in Fig. 7. Subsequently, these sub-grain boundaries were retarded by the Cu6Sn5 particles after a specific deformation level, and dislocations were continuously trapped into these boundaries, eventually resulting in the transformation of LAGBs into HAGBs, namely the formation of new recrystallized nuclei/grains. It should be noted that, besides the single Cu6Sn5 particle, the Cu6Sn5 clusters could also act as the heterogeneous sites for initiating nuclei. Those particle clusters were deemed to introduce severer lattice distortion in the surrounding matrix and to enhance the dislocations accumulation [28]. Thus, the Cu6Sn5 clusters can serve as effective nucleation sites, as shown in Fig. 7b. After the formation of the recrystallized nuclei, grain growth might subsequently occur. For the Cu6Sn5 particles which were sparsely spaced into the interior of Sn grains, once the energy

conditions for growth were met, the nuclei by PSN would grow by consuming the neighbouring deformed structure, leading to the boundary motion (growth) of the DRX grains. As a result, relatively large DRX grain could be formed. Note that the “energy conditions” referred to the combined effects caused by the driving forces and the retarding forces. The driving forces which dominated the boundary growth were the interface energy of the RDX grain boundaries, while the retarding forces were mainly resulted from the dispersed fine particles and solute atoms. However, if the criteria for nuclei growth was not met, the new nuclei would be maintained steady at small sizes. On the contrary, for the regions dominated by densely spaced Cu6Sn5 particles such as the original eutectic regions (highlighted in Fig. 6), numerous recrystallized nuclei might form simultaneously under a specific strain, resulting in a narrow distribution of fine grains. Also, the high number density of Cu6Sn5 particles acted as the obstacles to hinder the growth of the nuclei. Consequently, numerous closely packed fine recrystallized grains were established in the Cu6Sn5 particles dominant regions.

3.2.2.3. Boundary-induced nucleation. Fig. 7 provides the detailed microstructural features, which suggests another typical nucleation mechanism of DRX. Bunches of small DRX grains formed along the existing high-angle grain boundary and at the tri-junction of the boundaries, resulting in the formation of the necklace structures, as shown by the blue-colour ellipses in Fig. 7b. Necklace structures were the typical microstructures observed in DRX of other alloy systems like face-centred cubic and hexagonal close-packed metals and alloys [29–31], indicative of DRX from boundary-induced nucleation.

Usually, the initiation of DRX at grain boundaries has been explained based on the bulging mechanism [32,33]. That is, grain boundary shearing and/or sliding takes place at serrated grain boundaries developed at the early stage of deformation [29] and leads to the development of inhomogeneous or structure fluctuations near grain boundaries. The fluctuations prevent the boundary sliding or shearing under further deformation, dislocations then accumulate to increase the dislocation density gradients followed by sub-grains formation, and subsequently form HAGBs. The noticeable characteristic of this bulging mechanism is the appearance of the bulging boundaries, as well perceived by others [34]. However, this appears not the dominant mechanism in the present study of Sn-0.5wt.%Cu alloy since grain boundary bulging was barely detected in the structure after deformation. It is also observed in Fig. 7a that LAGBs and sub-grains were formed at the vicinities of the high-angle grain boundaries, as indicated by the dotted red-colour arrows. It is reminiscent of continuous dynamic recrystallization (CDRX) mechanism [35]. Although CDRX is defined as the global recovery of dislocations, higher dislocation density at mantle regions lead to formation of necklace structure at grain boundaries. The condition of plastic deformation in the present work involved relatively high temperatures and low strain rate, a homogeneous microstructure usually developed. CDRX occurs by the progressive accumulation of dislocations into LAGBs which increase their misorientation, and eventually HAGBs are formed. This mechanism has been reported in Al alloys [36] and micro-duplex stainless steel [37]. Here, the CDRX is believed the reason for the formation of necklace structure along the boundaries.

3.2.3. Twinning

In addition to the dislocation activities with respect to the formation, motion, and accumulation of LAGBs, twinning was observed as a readily existing deformation mechanism of the Sn-0.5wt.%Cu alloy under rolling. As aforementioned, a relative portion of boundaries with near-60° misorientation angles were identified and those boundaries were considered as twin boundaries associated with the {101) and {301) type twins. For accuracy, confirmation of the twin relationship was performed through analysis of the pole figures from the two neighbouring grains separated by a 60° boundary. The plot of the shared orientation relationship components, i.e. (101) or (301) planes in BCT β-Sn structure, reveals a shared point between the pole figures from twin and parent. Fig. 8 presents an example of a type of {101) instead of {301) twin relationship between the grain 1 and grain 2 on the ND + TD plane of the as-rolled Sn-0.5wt.%Cu alloy, evidenced by the shared point of {101), rather than {301) in the corresponding pole figures (Fig. 8b). This twin possessed the twin plane along {101) and the misorientation angle associated with this is 57.2° about ⟨100] axis. Moreover, the trace normal

of the {101) twin plane (dotted arrow in Fig. 8b) appeared not perpendicular to the trace of the highlighted twin boundary (Fig. 8a), indicating the twin boundary an incoherent twin boundary (ITB).

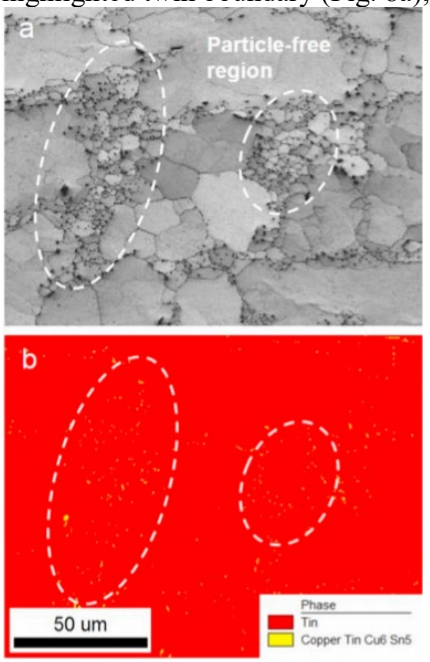

Fig. 6. (a) Image quality (IQ) map and (b) phase map of the rolled Sn-0.5wt %Cu alloy with its corresponding IPF referring to RD direction, showing the small-sized grains and large-sized grains in the particle-dominant region and particle-free region, respectively.

Fig. 9 shows an example of another type of twin on the RD + TD plane of the as-rolled Sn-0.5wt.%Cu alloy. The twin boundaries signified by ITB1–ITB5 were proved associated with the {301) twin planes, evidenced by the pole figures in Fig. 9b. Significantly, it is worthy pointing out that the five pairs of twins formed interior a same large deformed grain (the blue-colour elongated grain). The formation of these twins was very likely triggered by the strong local stress concentration. Also, these twins were, without exception, the {301) type twins but {101) type twins, might be indicative of the orientation-related formation of deformation twinning. It has been well established that deformation twinning is considerably dependent on the strain rate, deformation temperature, and the stacking fault energy (SFE) [38]. In the β-Sn system, owing to its multiple slip systems, dislocation-mediated slips such as dislocation climbing and cross-slip generally play essential roles in the deformation at moderate strain rates and room temperature [38]. However, deformation twinning has still been extensively observed and studied in the BCT Sn [15,39,40]. It is seen from Fig. 9a that a great deal of Cu6Sn5 particles and numerous particle-stimulated highly accumulated dislocations or sub-grain boundaries/LAGBs formed interior the deformed grain (the blue-colour elongated one). The strongly concentrated stress and the highly stored localized strain energy introduced by these LAGBs were prone to be released either through formation of HAGBs or twinning. Usually, formation of HAGBs is the common way to reduce the system energy at moderate strain rates. But once the external stress and the twining plans established a preferred geometrical orientation relationship, twinning could be initiated easily [39]. It might be for this reason that all the twins formed interior the same deformed grain were exclusively associated with the {301) type twins. That is, the orientation-related formation of deformation twinning matters.

In addition to the {301) twin related ITB1–5 on the RD + ND plane, the ITB6 was proved related to the {101) twin plane, evidenced by the pole figures in Fig. 9c. This {101) twin boundary (ITB6) was observed in a fully recrystallized grain instead of interior the deformed grain which was the case for the formation of ITB1–5. This phenomenon was associated with the nuclei nucleation process occurring near the highangle grain boundaries, which was reported in other metals/alloys under dynamic recrystallization [29]. It was based on the idea that DRX nuclei could be nucleated by bulging of some portions of serrated grain boundaries accompanied by the formation of twinning. The

boundaries of the DRX grains move outwards into the neighbouring deformed grain, leaving a twinning boundary in the back of the newly developed DRX grains. Thus, fine DRX grains could normally be found at the vicinity of the HAGBs. This is in line with the structure characterized in Fig. 9a in which a series of fine DRX grains formed at the boundary region between the highlighted DRX grain and the large elongated grain.

3.2.4. Recrystallization texture

Fig. 10 shows the inverse pole figures along the RD, extracted from all the recrystallized grains and the coarse recrystallized grains with grain sizes > 30 μm. It was seen from Fig. 10a that in recrystallized grains a clear ⟨110⟩//RD fibre texture was established, with the texture intensity of 3.2 times random (3.2TR), and an asymmetrical arc spanning from ⟨112⟩ passing through ⟨312⟩, and then reaching ⟨302⟩ was formed, with the corresponding texture intensities of 2.8, 2.8, and 2.3TR, respectively. The coarse recrystallized grains (> 30 μm)

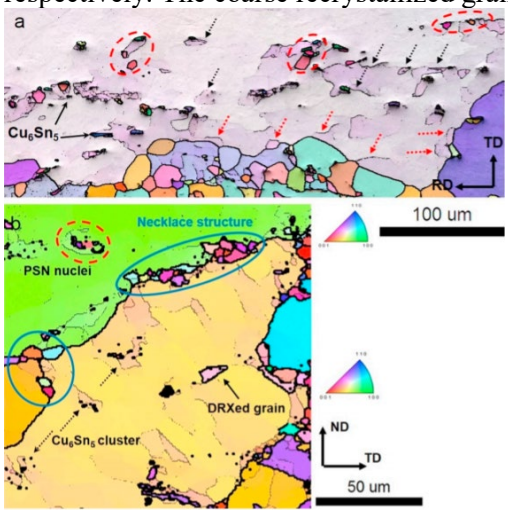

Fig. 7. (a) IPF + IQ map on the RD + TD plane, and (b) IPF map on the ND + TD plane of the rolled Sn-0.5wt%Cu alloy, showing the PSN phenomenon and boundary-induced nucleation. The HAGBs (> 15°) and LAGBs (2–15°) presented by thick and thin black lines, respectively.

displayed a slightly different textural feature in comparison with the whole recrystallized grains, presenting a stronger ⟨110⟩//RD (5.0TR) and ⟨312⟩//RD (3.5TR) texture but a weaker ⟨112⟩//RD (2.7) texture and the same intensity (2.3RT) of the ⟨302⟩//RD texture (Fig. 10b). To further analysis the initial texture of the recrystallized nuclei, the texture features from the fine grains (< 30 μm) was investigated solely. Fig. 11a shows the IPF map differentiated from Fig. 4a, illustrating the orientations and distribution of the fine recrystallized grains with the grain size smaller than 30 μm. Fig. 11b and c present the corresponding inverse pole figure and (001) pole figure along the RD, respectively, suggesting a manifest textural figure for the fine DRX nuclei/grains. It was found that a near-⟨001⟩//RD fibre texture was established for the fine DRX grains, which was evidenced by the fact that most of the fine grains/nuclei had the c-axes closely aligned to the RD, as indicated by the IPF (texture intensity: 2.7TR) and PF (texture intensity: 7.5TR) (Fig. 11b and c). Therefore, it was generally established that the nuclei possessed a ⟨001⟩//RD fibre texture, while the overall recrystallized grain had a co-existence of the arc ⟨112⟩//RD-⟨312⟩//RD-⟨302⟩//RD and the ⟨110⟩//RD fibre, indicating the occurrence of transformation of the orientation from the ⟨001⟩//RD texture to others such as the ⟨110⟩//RD texture after grain growth.

As stated, the fine recrystallized grains/nuclei were mainly originated from PSN despite of the occasional existence of small portion of nucleation along the initial grain boundaries, it is thus reasonably deduced that the Cu6Sn5 particles could be closely related to the formation of strongly oriented nuclei (⟨001⟩//RD). This was also observed in nickel alloys where the nuclei formed near the silica particles were found to be oriented as well [41].

It was reported that the Cu6Sn5 particles tended to be distorted in such a way that the axes of Cu6Sn5 particle rods were aligned to the rolling direction [8]. This might provide preferential orientation configurations between the stresses and the Cu6Sn5/β-Sn interfaces, which could facilitate the formation of ⟨001⟩//RD nuclei. Those oriented nuclei might not necessarily grow into coarse grains with the ⟨001⟩// RD orientation remained, as on one hand, the motion of nuclei boundaries could be hindered or pinned by the densely distributed Cu6Sn5 particles. On the other hand, even if there were no obstacles retarding the nuclei growth, such as the nuclei formed in the interior of grains, the specific strong orientation (⟨001⟩//RD) of the nuclei could still be weakened by the oriented growth of other nuclei such as those with orientation of ⟨110⟩//RD. This relies on the growth advantages of the specific PSN orientations mostly due to their close to a certain relationship with the deformed β-Sn matrix. For example, a growth advantage of a near 40° ⟨111⟩ orientation relationship in Al-1.8wt.%Cu [42], and a 24° ⟨150⟩ orientation relationship in aluminium crystals [43] were observed. Although the preferential orientation relationship in the present alloy is still not clear, the oriented growth was very likely the reason for the transformation of oriented texture from ⟨001⟩//RD into ⟨110⟩//RD. However, further works with reference to the preferential growth orientation in the present Sn-Cu alloy under the specified processing configurations need to be performed for profound understanding in this respect.

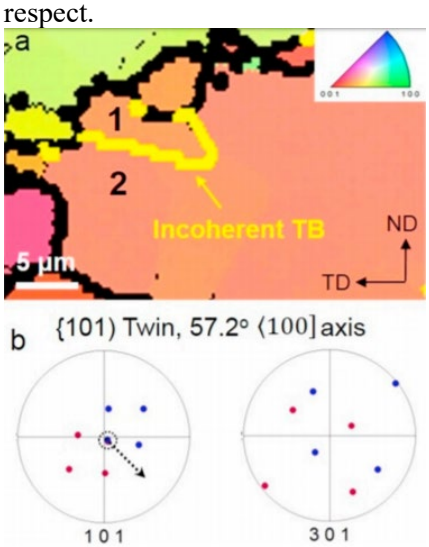

Fig. 8. (a) IPF map showing a typical {101} type twin on the ND + TD plane of the rolled Sn-0.5wt%Cu alloy, and (b) the (101) and (301) pole figures from grain 1 and grain 2, demonstrating a {101) twin relationship between the two grains. The HAGBs (> 15°) and LAGBs (2–15°) presented by thick and thin black lines, respectively. Yellow-coloured thick line showing a 57.2° incoherent twin boundary (ITB). (For interpretation of the references to colour in this figure legend, the reader is referred to the web version of this article.)

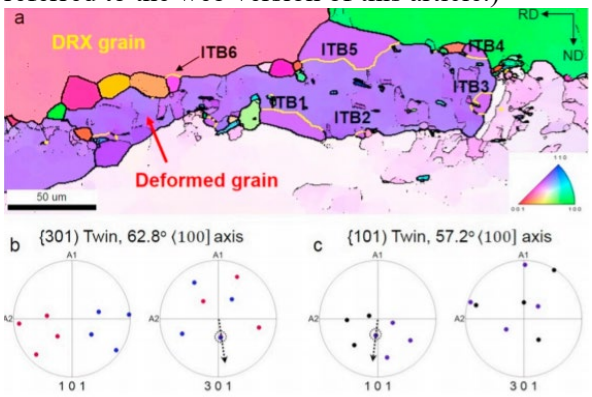

Fig. 9. (a) IPF map on the RD + ND plane of the rolled Sn-0.5wt%Cu alloy, showing the two types of {301) and {101} twins, with the corresponding incoherent twin boundaries ITB1–5 and ITB6, respectively, (b) (101) and (301) pole figures from grain pairs isolated by ITB1–5, (c) (101) and (301) pole figures from grain-pair separated by ITB1.

4. Conclusions

In the present study, the Sn-0.5wt.%Cu alloy was investigated after rolling at moderate strain rates. The microstructure features including grain/sub-grain boundaries, dynamic restoration of DRV and DRX, twinning, and recrystallization texture were extensively characterized through EBSD technique. Main conclusions could be drawn as following:

(1) The Sn-0.5wt.%Cu alloy after rolling at room temperature showed a manifest bimodal grain structure containing over 97% (frequency) of fine grains < 30 μm and small portion of coarse grains in the range of 50–150 μm.

(2) DRX played a dominant role in the deformation. Particle-stimulated nucleation (PSN) phenomenon by the Cu6Sn5 particles/clusters was the main DRX mechanism. And, the boundary-induced nucleation was detected as another DRX mechanism, which was associated with the continuous dynamic recrystallization (CDRX).

(3) {301) and {101) type twins were extensively observed as an effective deformation mechanism during rolling. The formation of the {301} twin might be closely related to the orientation, which resulted from a specific orientation relation between the stress and the orientation of the deformed grains.

(4) The fine DRX nuclei/grains displayed the ⟨001⟩//RD fibre texture, which was associated with the specific orientation relationship between the external stress and the Cu6Sn5/β-Sn interface. The ⟨001⟩//RD fibre texture in fine DRX nuclei was weakened and ⟨110⟩//RD fibre texture became strengthened with grain growth, which could be ascribed to the growth advantages of the specific orientation relationships.

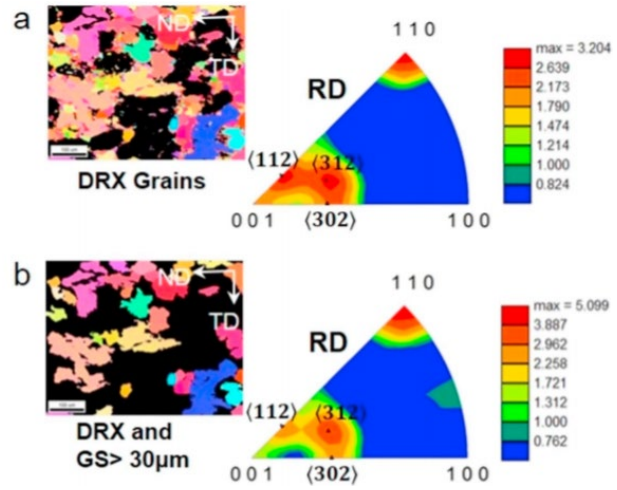

Fig. 10. Inverse pole figures (IPF) maps of on the ND + TD plane of the rolled Sn-0.5wt%Cu alloy, showing (a) the recrystallized (DRX) grains and (b) DRX grain larger than 30 μm.

Fig. 11. (a) Inverse pole figure (IPF) map on the ND + TD plane of the rolled Sn-0.5wt%Cu alloy, showing the recrystallized grains with grain size smaller than 30 μm, (b) corresponding IPF and (c) (001) pole figure.

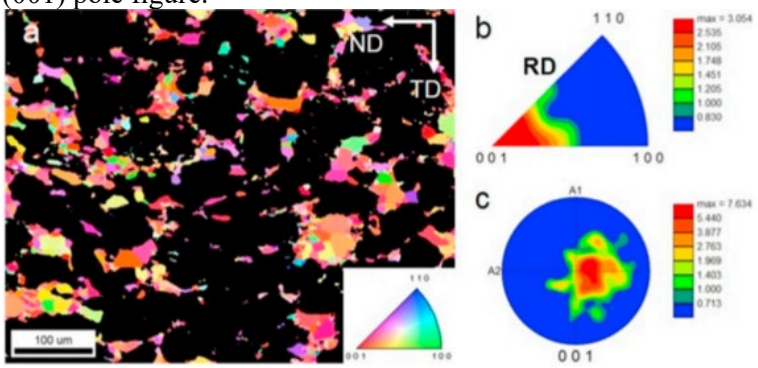

Fig. 11. (a) Inverse pole figure (IPF) map on the ND + TD plane of the rolled Sn-0.5wt%Cu alloy, showing the recrystallized grains with grain size smaller than 30 μm, (b) corresponding IPF and (c) (001) pole figure.

Acknowledgment

Financial support from the National Aerospace Technology Exploitation Programme (NATEP) and Chemring Energetics UK [grant number WEAF058] is gratefully acknowledged.

References

[1] C.S. Kaira, S.S. Singh, A. Kirubanandham, N. Chawla, Microscale deformation behaviour of bi crystal boundaries in pure tin (Sn) using micropillar compression, Acta Mater. 120 (2016) 56–67.
[2] M. Abtew, G. Selvaduray, Lead-free solders in microelectronics, Mater. Sci. Eng. R. Rep. 27 (2000) 95–141.
[3] G. Liu, S. Ji, Effect of Bi on the microstructure and mechanical properties of Sn-Zn alloys processed by rolling, Mater. Charact. 137 (2008) 39–49.
[4] Y.F. Gao, C.Q. Cheng, Z.H.A.O. Jie, L.H. Wang, X.G. Li, Electrochemical corrosion of Sn-0.75 Cu solder joints in NaCl solution, Trans. Nonferrous Metals Soc. China 22 (2012) 977–982.
[5] Graham, J.A. & Ensign-Bickford Co. Reactive products having tin and tin alloy liners and sheaths. U.S. Patent 5,827,995, 1998.
[6] Rodney, S., Barr, L.H. & Teledyne Mccormick Selph. Tin alloy sheath material for explosive-pyrotechnic linear products. U.S. Patent 5,333,550, 1994.
[7] Huang Y.S. et al. Non-lead metal material and application of non-lead metal material to cord type initiating explosive devices, CN 102560194A, 2012.
[8] G. Liu, S. Ji, L. Grechcini, A. Bentley, Z. Fan, Microstructure and mechanical properties of Sn-Cu alloys for detonating and explosive cords, Mater. Sci. Technol. 33 (2017) 1907–1918.
[9] G.R. Moreno, B.L. Silva, A.A. Bogno, H. Henein, J.E. Spinelli, Microstructureproperty relations in as-atomized and as-extruded Sn-Cu (-Ag) solder alloys, J. Alloys Compd. 680 (2016) 259–267.
[10] E.S. Freitas, W.R. Osório, J.E. Spinelli, A. Garcia, Mechanical and corrosion resistances of a Sn-0.7 wt.% Cu lead-free solder alloy, Microelectron. Reliab. 54 (2014) 1392–1400.
[11] J.H. Pang, B.S. Xiong, T.H. Low, Low cycle fatigue study of lead free 99.3 Sn-0.7 Cu solder alloy, Int. J. Fatigue 26 (2004) 865–872.
[12] C.L. Wu, M.L. Huang, Creep behaviour of eutectic Sn-Cu lead-free solder alloy, J. Electron. Mater. 31 (2002) 442–448.
[13] Noddin, G.A., EI du Pont de Nemours & Co. Non-rupturing detonating cords. U.S. Patent 3,311,056, 1967.
[14] S.K. Seo, S.K. Kang, D.Y. Shih, H.M. Lee, The evolution of microstructure and microhardness of Sn-Ag and Sn-Cu solders during high temperature aging, Microelectron. Reliab. 49 (2009) 288–295.
[15] L.P. Lehman, Y. Xing, T.R. Bieler, E.J. Cotts, Cyclic twin nucleation in tin-based solder alloys, Acta Mater. 58 (2010) 3546–3556.
[16] H. Kih, Incorporation of slip dislocations in mechanical twins of tin crystals, J. Phys. Soc. Jpn. 18 (1963) 1122–1132.
[17] C.M. Sellars, Recrystallization of metals during hot deformation, Philos. Trans. R. Soc. Lond. A 288 (1978) 147–158.
[18] F. Haessner, Recrystallization of Metallic Materials, Dr. Riederer Verlag, GmbH, Stuttgart, 1978.
[19] H.J. McQueen, J.J. Jonas, Recovery and recrystallization during high temperature deformation, Treatise on Materials Science & Technology, 1975, pp. 393–493.
[20] S.I. Wright, M.M. Nowell, D.P. Field, A review of strain analysis using electron backscatter diffraction, Microsc. Microanal. 17 (2011) 316–329.
[21] F.J. Humphreys, M. Hatherly, Recrystallization and Related Annealing Phenomena, Elsevier, 2012.
[22] P. Darbandi, T.R. Bieler, F. Pourboghrat, T.K. Lee, Crystal plasticity finite-element analysis of deformation behaviour in multiple-grained lead-free solder joints, J. Electron. Mater. 42 (2013) 201–214.

[23] N.S. Brar, W.R. Tyson, Elastic and plastic anisotropy of white tin, Can. J. Phys. 50 (1972) 2257–2264.
[24] T.R. Bieler, A.U. Telang, Analysis of slip behaviour in a single shear lap lead-free solder joint during simple shear at 25 C and 0.1/s, J. Electron. Mater. 38 (2009) 2694–2701.
[25] F.J. Humphreys, The nucleation of recrystallization at second phase particles in deformed aluminium, Acta Metall. 25 (1977) 1323–1344.
[26] R.D. Doherty, et al., Current issues in recrystallization: a review, Mater. Sci. Eng. A 238 (1997) 219–274.
[27] R.A. Shahani, T.W. Clyne, Recrystallization in fibrous and particulate metal matrix composites, Mater. Sci. Eng. A 135 (1991) 281–285.
[28] J.D. Robson, D.T. Henry, B. Davis, Particle effects on recrystallization in magnesium-manganese alloys: particle-stimulated nucleation, Acta Mater. 57 (2009) 2739–2747.
[29] A.M. Wusatowska-Sarnek, H. Miura, T. Sakai, Nucleation and microtexture development under dynamic recrystallization of copper, Mater. Sci. Eng. A 323 (2002) 177–186.
[30] R.R. Eleti, T. Bhattacharjee, L. Zhao, P.P. Bhattacharjee, N. Tsuji, Hot deformation behaviour of CoCrFeMnNi FCC high entropy alloy, Mater. Chem. Phys. 210 (2018) 176–186.
[31] A. Imandoust, et al., Nucleation and preferential growth mechanism of recrystallization texture in high purity binary magnesium-rare earth alloys, Acta Mater. 138 (2017) 27–41.
[32] J.E. Bailey, P.B. Hirsch, The recrystallization process in some polycrystalline metals, Proc. R. Soc. Lond. A 267 (1962) 11–30.
[33] D. Ponge, G. Gottstein, Necklace formation during dynamic recrystallization: mechanisms and impact on flow behaviour, Acta Mater. 46 (1998) 69–80.
[34] B. Shen, L. Deng, X. Wang, A new dynamic recrystallisation model of an extruded Al-Cu-Li alloy during high-temperature deformation, Mater. Sci. Eng. A 625 (2015) 288–295.
[35] A. Rollett, F.J. Humphreys, G.S. Rohrer, M. Hatherly, Recrystallization and Related Annealing Phenomena, Elsevier, 2004.
[36] R. Kaibyshev, K. Shipilova, F. Musin, Y. Motohashi, Continuous dynamic recrystallization in an Al-Li-Mg-Sc alloy during equal-channel angular extrusion, Mater. Sci. Eng. A 396 (2005) 341–351.
[37] K. Tsuzaki, X. Huang, T. Maki, Mechanism of dynamic continuous recrystallization during superplastic deformation in a microduplex stainless steel, Acta Mater. 44 (1996) 4491–4499.
[38] J.W. Christian, S. Mahajan, Deformation twinning, Prog. Mater. Sci. 39 (1995) 1–157.
[39] B. Chalmers, The twinning of single crystals of tin, Proc. Phys. Soc. 47 (1935) 733–746.
[40] S. Maruyama, Dynamic behaviour of twinning in tin crystals at various temperatures and strain rates, J. Phys. Soc. Jpn. 15 (1960) 1243–1251.
[41] F.J. Humphreys, Particle stimulated nucleation of recrystallization at silica particles in nickel, Scr. Mater. 43 (2000) 591–596.
[42] O. Engler, J. Hirsch, K. Lücke, Texture development in Al-1.8 wt% Cu depending on the precipitation state-II. Recrystallization textures, Acta Metall. Mater. 43 (1995) 121–138.
[43] M. Ferry, F.J. Humphreys, The deformation and recrystallization of particle-containing {011} ⟨100⟩ aluminium crystals, Acta Mater. 44 (1996) 3089–3103. G. Liu and S. Ji Materials Characterization 150 (2019) 174–183 183